Tunable spin-orbit coupling and magnetic superstripe phase in a Bose-Einstein condensate

Xi-Wang Luo ⬤ and Chuanwei Zhang*

Department of Physics, The University of Texas at Dallas, Richardson, Texas 75080-3021, USA

Superstripe phases in Bose-Einstein condensates (BECs), possessing both crystalline structure and superfluidity, open a new avenue for exploring exotic quantum matters—supersolids. However, conclusive detection and further exploration of a superstripe is still challenging in experiments because of its short period, low visibility, fragility against magnetic-field fluctuation, or short lifetime. Here we propose a scheme in a spin-orbit coupled BEC which overcomes these obstacles and generates a robust magnetic superstripe phase, with only spin-density (no total density) modulation due to the magnetic translational symmetry, ready for direct real-space observation. In the scheme, two hyperfine spin states are individually Raman coupled with a largely detuned third state, which induce a momentum-space separation between two lower band dispersions, yielding an effective spin-1/2 system with tunable spin-orbit coupling and Zeeman fields. Without effective Zeeman fields, spin-dependent interaction dominates, yielding a magnetic superstripe phase with a long tunable period and high visibility. Our scheme provides a platform for observing and exploring exotic properties of superstripe phases as well as novel physics with tunable spin-orbit coupling.

I. INTRODUCTION

In supersolids, crystalline and superfluidity orders are formed through spontaneously breaking continuous translational and $U(1)$ gauge symmetries [1]. The concept of supersolidity was originally discussed in solid ^{4}He [2,3], and later generalized to other superfluid systems that spontaneously form spatial periodicity. In particular, ultracold atomic gases provide a powerful platform for exploring quantum phases with supersolidlike properties [4–10]. For instance, a superstripe phase with spontaneously formed periodic density modulation has been theoretically proposed for a spin-orbit (SO) coupled Bose-Einstein condensate (BEC) with anisotropic spin interactions [11–15]. In this context, the recent experimental realization of SO coupling in ultracold atoms [16–27] paves a promising path for the observation and exploration of the long-sought supersolid phases. Here the pseudospin states could be formed by either two atomic hyperfine ground states [28–34] or two sites of a double-well optical lattice [35]. For the latter case, the crystalline structures of a BEC have been indirectly observed recently using Bragg reflection [36].

There are a few major obstacles [37–39] for conclusive observation and further exploration of superstripe phases in a SO coupled BEC.

(i) A superstripe is formed by the superposition of two plane waves separated by a large momentum, leading to a short period at the order of optical wavelength for the density modulation [16,17].

(ii) A superstripe phase is energetically unfavorable by density interaction g_0 due to its total density modulation, and therefore could only exhibit a low visibility and exist in

a small parameter region favored by weak spin interaction [12,14].

(iii) The superstripe phase for hyperfine state pseudospins is fragile against magnetic-field fluctuation because the relative energy between two spin states is sensitive to the magnetic field [13,18,19].

(iv) The superstripe phases for double-well lattice pseudospins (where SO coupling is realized by additional moving lattices) or dipole gases have a short lifetime [8–10,36].

In this paper, we propose that all these obstacles can be completely overcome by engineering an effective spin-1/2 subsystem with tunable SO coupling in a spin-1 BEC (we use atomic hyperfine-state pseudospins to avoid heatings) [40–43], leading to a promising scheme for in-depth investigation of supersolidity. Our main results are the following.

(i) We propose a generic and experimentally feasible scheme for generating an effective spin-1/2 system with tunable SO coupling through two individual Raman couplings of two spin states ($|\uparrow\rangle$, $|\downarrow\rangle$) with a third higher-energy state ($|0\rangle$), which induce a momentum separation between two lower band dispersions, yielding SO coupling. The SO coupling strength can be widely tuned by varying laser and microwave intensities, in contrast to fixed SO coupling strength determined by the laser geometry in previous experiments [16].

(ii) Because the SO coupling is induced by the Raman coupling with the third state, it can exist without an effective transverse field, where the total density modulation vanishes (due to magnetic translational symmetry) even when both band minima are occupied by the BEC. In this case, the spin interaction g_2, instead of density interaction g_0, dominates the phase diagram, leading to a high-visibility ($\approx 100\%$) magnetic superstripe phase with only spin-density modulation. Depending on the SO coupling strength, the superstripe period is tunable up to $\approx 5\,\mu$m, which can be directly imaged in the real space. Finally, the relative energy between two band
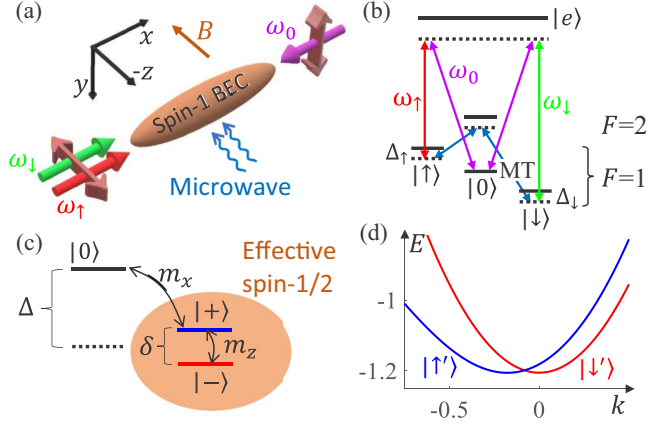

FIG. 1. (a) Experimental scheme to generate SO coupling for an effective spin-1/2 system using a spin-1 BEC. The bias field B is along the z direction. (b) The corresponding two-photon Raman transitions and microwave transitions (MT) between three hyperfine spin states. (c) Mapping to an effective spin-1/2 system, with spin states $|\pm\rangle = \frac{1}{\sqrt{2}}(|\uparrow\rangle \pm |\downarrow\rangle)$, $\Delta = (\Delta_\uparrow + \Delta_\downarrow)/2$, and $m_z = (\Delta_\uparrow - \Delta_\downarrow)/2$. (d) Two lower bands for $m_x = 1$, $m_z = 0$, $\delta = 0.205$, and $\Delta = -1$.

minima is insensitive to magnetic-field fluctuations, making the superstripe phase robust in experiments.

(iii) Beside superstripe phases, we find a rich phase diagram with other phases in different parameter regions.

II. EXPERIMENTAL SCHEME AND HAMILTONIAN

We consider an experimental setup shown in Fig. 1(a), which is similar to that in a recent experiment [26] but with different laser configuration and additional microwave fields. Three Raman lasers are employed to couple hyperfine states $|\uparrow, \downarrow\rangle$ with $|0\rangle$ in the $F = 1$ manifold of ^{87}Rb atoms [see Fig. 1(b)], with $2k_R$ momentum transfer. $|\downarrow\rangle$ and $|\uparrow\rangle$ are coupled by a two-photon microwave transition via an intermediate virtual state $|F = 2, m_F = 0\rangle$ [44–46] with zero-momentum transfer. After a unitary transformation $U = \exp(i2k_Rx)|0\rangle\langle0|$ that only transforms state $|0\rangle$ to a quasi-momentum basis, the resulting single-particle Hamiltonian becomes

$$H_0 = \hat{k}^2 - (4\hat{k} + 4)(F_z^2 - 1) + \Delta F_z^2$$
$$+ \sqrt{2}m_xF_x + m_zF_z + \delta(F_x^2 - F_y^2). \quad (1)$$

Here we set $\hbar = 1$ and use the energy and momentum units $\frac{k_R^2}{2m}$ and k_R. F_i ($i = x, y, z$) are spin vectors and $4\hat{k}F_z^2$ describes the spin-tensor-momentum coupling [43]. m_x (δ) is the Raman (microwave) coupling strength between $|0\rangle$ and $|\uparrow, \downarrow\rangle$ ($|\uparrow\rangle$ and $|\downarrow\rangle$), which can be tuned with high precision. The phase difference between two Raman lasers with frequencies $\omega_\uparrow$ and $\omega_\downarrow$ is locked to the same value as that between two microwave fields such that m_x and δ become real and positive by gauging out irrelevant phases. m_z and Δ are linear and quadratic Zeeman fields that can be tuned by laser detunings.

III. TUNABLE SO COUPLING STRENGTH

We consider a large $\Delta \ll 0$ such that low-energy dynamics are mainly characterized by spin states $|\uparrow\rangle$ and $|\downarrow\rangle$ with two band minima near $k = 0$ [see Figs. 1(c) and 1(d)]. By hybridizing $|+\rangle$ [$|\pm\rangle \equiv \frac{1}{\sqrt{2}}(|\uparrow\rangle \pm |\downarrow\rangle)$] with $|0\rangle$ [see Fig. 1(c)] for state $|\uparrow'\rangle$, the Raman coupling m_x induces a momentum shift for the $|\uparrow'\rangle$ band with band minimum $k_m < 0$ [see Fig. 1(d)]. The band for $|\downarrow'\rangle \equiv |-\rangle$ is unaffected by m_x. To restore the degeneracy between two band minima, a two-photon microwave transition with $\delta > 0$ is used to tune their relative energy, forming an effective spin-1/2 system [see Fig. 1(d)]. Here δ is crucial because the $|\downarrow'\rangle$ band would be always higher than the $|\uparrow'\rangle$ band without δ [43].

The low-energy effective Hamiltonian in the basis $\{|\uparrow'\rangle, |\downarrow'\rangle\}$ can be written as

$$H_{\text{eff}} = \begin{bmatrix} \eta(k - k_m)^2 & 0 \\ 0 & k^2 \end{bmatrix} + B_z\sigma_z + B_x\sigma_x, \quad (2)$$

leading to a SO coupling $\eta k_m k\sigma_z$. The effective "detuning" B_z and "Raman coupling" B_x between $|\uparrow'\rangle$ and $|\downarrow'\rangle$ bands can be tuned by δ and m_z, respectively (see the Appendix). η is the mass ratio between $|\uparrow'\rangle$ and $|\downarrow'\rangle$ and k_m characterizes the SO coupling strength, which can be tuned by varying Raman laser intensities (i.e., m_x). In contrast, the SO strength is preset by Raman laser geometry [34] in previous experiments and its modulation through periodic fast modulation of laser intensities [47–49] may lead to significant heating issues and complex interaction effects.

Our scheme for tunable one-dimensional (1D) SO coupling only relies on the existence of three hyperfine ground states that can be coupled with each other, therefore it can be applied to other alkali-metal (e.g., potassium) and alkaline-earth(-like) atoms (e.g., strontium and ytterbium). The corresponding laser configurations could be slightly different (see the Appendix).

IV. INTERACTING PHASE DIAGRAM

In the presence of atomic interaction, the effective spin-1/2 system with tunable SO coupling provides a path for realizing superstripe phases with long period and high visibility. For the simplicity of the presentation and accurate description of the results, we, however, still use the original spin-1 Hamiltonian (1) for our calculation.

The interaction energy density can be expressed as (see the Appendix)

$$\varepsilon_{\text{int}} = \frac{1}{V}\int dx\left[\frac{g_0}{2}n_{\text{tot}}^2 + g_2n_0(n_\uparrow + n_\downarrow) + \frac{g_2}{2}\mathcal{F}_z^2\right], \quad (3)$$

where V is the system volume and n_{tot} and n_i ($i = 0, \uparrow, \downarrow$) are the total and spin densities, with $\mathcal{F}_z \equiv n_\uparrow - n_\downarrow$ the polarization and g_0 and g_2 the density- and spin-interaction strengths. Under the Gross-Pitaevskii (GP) approximation, we adopt a variational ansatz as the general superposition of two plane waves around two band minima:

$$\Psi = \sqrt{\bar{n}}(|c_1|\chi_1e^{ik_1x} + |c_2|\chi_2e^{ik_2x+i\alpha}), \quad (4)$$

which is normalized by the average particle number density $\bar{n} = V^{-1}\int dx\Psi^\dagger\Psi$, with three-component spinors
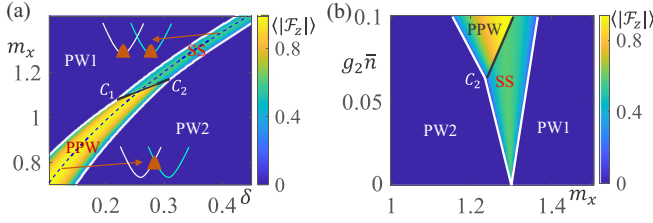
FIG. 2. (a) Phase diagram in the m_x-δ plane with $g_2\bar{n} = -0.05$, $\Delta = -1$, and $m_z = 0$. The color bar shows the property of the polarization density (average of its absolute value). (b) Phase diagram in the m_x-g_2 plane with $\delta = 0.35$; other parameters are the same as in (a). Black (white) solid lines correspond to first-order (second-order) phase transitions.

$\chi_j = (\cos\theta_j \cos\phi_j, -\sin\theta_j, \cos\theta_j \sin\phi_j)^T$ and $|c_1|^2 + |c_2|^2 = 1$. The ground state is determined by minimizing the total-energy density

$$\varepsilon_{\text{tot}} = \varepsilon_{\text{int}} + \frac{1}{V}\int dx \Psi^\dagger H_0 \Psi \qquad (5)$$

with respect to eight variational parameters $|c_1|$, k_1, k_2, θ_1, θ_2, ϕ_1, ϕ_2, and α (see the Appendix). The phase diagram can be characterized by the atomic total density n_{tot}, spin density n_i, and polarization $\langle F_z \rangle$ which can be measured directly in experiments. We also obtain the ground states by directly simulating the GP equation numerically, which are in good agreement with the variational results.

We first consider $m_z = 0$, where the spin states of the two lower bands are orthogonal (i.e., $\langle \chi_1 | \chi_2 \rangle = 0$ for $B_x = 0$). Therefore, the total density is always a constant, and the density interaction g_0 plays no role for the phase diagram. The spin interaction g_2 tends to lower the energy by occupying both band minima, leading to a superstripe ground state. The phase diagram obtained from the variational method for ferromagnetic spin interaction (e.g., ^{87}Rb with $g_2 < 0$) is shown in Fig. 2(a) as a function of Raman couplings m_x and δ. There are four phases: the plane-wave phase PW1 (PW2) with zero-spin polarization (i.e., $F_z = 0$) and single momentum occupation at the left (right) band minimum; the polarized plane-wave phase PPW with uniform spin polarization (i.e., $F_z \neq 0$) and single momentum occupation at the barrier between two band minima; and the magnetic superstripe phase SS with striped spin polarizations F_z (total density is uniform) and momentum occupations at both band minima [see the inset in Fig. 2(a)]. The plane-wave phases preserve the continuous translational symmetry with $\hat{T}_d |\Psi\rangle = e^{ik_1 d}|\Psi\rangle$, where $\hat{T}_d$ is the translation operator. For the SS phase, we have $\hat{T}_d |\Psi\rangle = \Lambda_d |\Psi\rangle$ with Λ_d a spatial-independent unitary matrix because of $\langle \chi_1 | \chi_2 \rangle = 0$. In particular, we have $\Lambda_d = e^{ik_1 d}|\chi_1\rangle\langle\chi_1| + e^{ik_2 d}|\chi_2\rangle\langle\chi_2|$. This means that the SS phase breaks the translational symmetry but preserves a magnetic translational symmetry $\hat{T}_m |\Psi\rangle = |\Psi\rangle$ with $\hat{T}_m = \Lambda_d^\dagger \hat{T}_d$. This magnetic translational symmetry is responsible for the uniform total density [since $n_{\text{tot}}(x+d) = |\hat{T}_m \Psi|^2 = |\Psi|^2 = n_{\text{tot}}(x)$].

Both PPW and SS phases result from the ferromagnetic spin interaction, and the total energy is minimized by generating non-zero-spin polarizations F_z (uniform in PPW and striped in SS). We note that only state $|0\rangle$ is transformed to the

quasimomentum basis, therefore the spin-density modulation F_z in the SS phase is unaffected after transforming back to the real mechanical momentum. The uniform polarization F_z in the PPW phase can be either positive or negative due to the spontaneous breaking of the discrete Z_2 symmetry between states $|\uparrow\rangle$ and $|\downarrow\rangle$. In the supersolid-ordered SS phase, $n_\uparrow$ and $n_\downarrow$ exhibit out-of-phase density modulations (therefore leading to a non-zero-spin-polarization modulation F_z) that spontaneously break the continuous translational symmetry due to the arbitrariness of relative phase α between two k states. We can always choose the relative strength between the Raman and microwave couplings such that two band minima are degenerate [see the dashed line in Fig. 2(a)]; therefore, the SS phase can exist in a long ribbon along the degenerate line in the m_x-δ plane.

For a strong Raman coupling m_x, where two band minima are well separated [the upper part in Fig. 2(a)], the ground state prefers a plane wave (PW1) at the left band minimum when the microwave transition δ is weak. As we increase δ [which would raise (lower) the left (right) band minimum], the BEC starts to partially occupy the right band minimum, undergoing a second-order phase transition to the magnetic superstripe phase (SS) where both minima are populated. By further increasing δ, the population of the right (left) minimum increases (decreases) until another second-order phase transition occurs where the BEC is fully transferred to the low-energy right minimum (PW2).

For weak Raman coupling m_x [the lower part of the diagram of Fig. 2(a)], the two band minima are too close in momentum space to form the magnetic superstripe phase. If the system starts at the PW1 phase, it undergoes a second-order phase transition to the PPW phase as δ increases, where the BEC would not partially occupy the right band minimum but, instead, starts to occupy two lower bands at the same momentum, generating a uniform spin polarization. Therefore, the BEC stays in a plane-wave state and shifts towards the right band minimum as a whole, where a second-order phase transition to PW2 occurs. The transition between SS and PPW phases is of first order, with their phase boundary ending at two triple points $C_{1,2}$, as shown in Fig. 2(a). Compared with the SS phase, the PPW phase has a higher single-particle energy, but the total energy is favorable due to lower spin-interaction energy from its uniform spin polarization. As a result, the system prefers the PPW phase for weak Raman coupling m_x where the SO coupling is weak and the band barrier is low. For conventional SO coupled spin-1/2 systems, atoms may condense at the barrier maximum only for very strong Raman coupling or interaction [14].

In Fig. 2(b) we plot the phase diagram in the g_2-m_x plane with a fixed δ. We see that the areas of PPW and SS phases shrink as $|g_2|$ decreases, and the PPW phases in the weak SO coupling region are replaced by the SS phase as g_2 decreases. Therefore, the SS phase can have even longer period for weaker spin interaction. In Fig. 2(b) with spin interaction $g_2\bar{n} = -0.05$, the superstripe period can be up to around 3.8 μm (see the Appendix). For $g_2\bar{n} = -0.01$, the period can be greater than 5 μm, as in Fig. 3(a). Due to the uniform total density (n_0 is also uniform), the density interaction g_0 is irrelevant, and the spin interaction g_2 can lead to high-visibility ($\approx 100\%$) spin modulations in
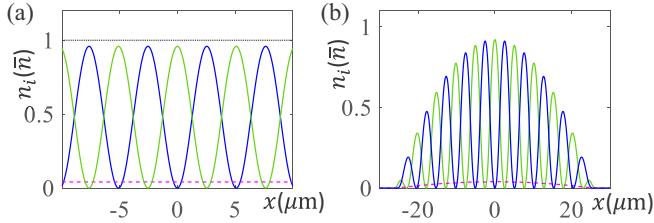
FIG. 3. Spin-density modulations in the SS phase. (a) Ground state obtained from the variational ansatz for a nontrapped BEC. (b) Ground state for a trapped BEC (with trapping frequency 50 Hz) obtained by directly solving the GP equation. Common parameters: $g_2\bar{n} = -0.01$, $g_0 = 200|g_2|$, $\delta = 0.18$, and $m_x = 0.938$ (m_x is chosen to obtain two degenerate band minima), and other parameters are the same as in Fig. 2(a). Blue (black) solid, green (light gray) solid, black dotted, and purple dashed lines correspond to $n_\uparrow$, $n_\downarrow$, n_0, and $n_{\rm tot}$, respectively. Raman lasers with 790-nm wavelength (typical for alkali-metal atoms) are used.

FIG. 4. (a) Phase diagram in the m_z-g_2/g_0 plane with $m_x = 1.2$, $\Delta = -1$, and $g_2\bar{n} = -0.01$. The color bar shows the averaged polarization $\langle F_z \rangle$. Though the SS phase can exist in a large interval of δ, here PW1 is sensitive to δ and we use $\delta = 0.298$ to make the PW1 region large. (b) Phase diagram in the m_z-δ plane with $m_x = 2$, $\Delta = 0$, $g_2\bar{n} = -0.01$, and $g_0 = 200|g_2|$. Color bar shows averaged momentum. The SS-PW2 transition changes from second order [green (light gray) line] to first order (black line) at the point marked by a star.

the SS phase, where the spin densities $n_{\uparrow,\downarrow}$ show out-of-phase modulation with a long period and high visibility. In Fig. 3(b) we show the density distributions in the presence of a realistic harmonic trap, which are obtained by numerical simulation of the GP equation directly. Such long-period (≈ 5 μm) and high-visibility ($\approx 100\%$) magnetic superstripes can be directly detected by real-space imaging [50–52]. We emphasize that here the long-period, high-visibility superstripe phase is the ground state possessing true supersolidity, which is different from the dynamically generated excited superstripe state [43].

V. ZEEMAN FIELD EFFECTS

So far we have focused on the case with zero linear Zeeman field $m_z = 0$. In a realistic experiment, though the detunings of laser frequencies can be tuned with high accuracy, the magnetic-field fluctuation would lead to a nonzero m_z. Therefore, the robustness of the superstripe phase against Zeeman field fluctuation is very important. In a conventional SO coupled spin-1/2 system [16,19], the spin states are represented directly by the hyperfine states, leading to two band minima the energies of which are sensitive to magnetic fields [14]. The superstripe phase is stable only in a narrow width $|m_z| \lesssim g_2\bar{n}/4$, which requires extreme control of ambient magnetic-field fluctuations that is very challenging [36]. In our system, m_z acts like an effective Raman coupling which opens a band gap at the crossing point between two lower bands. We find that the SS phase could be very robust against such effective Raman coupling.

In the presence of m_z, the spin states at the two band minima are no longer orthogonal, and the SS phase now possesses both spin-density and total density modulations (see the Appendix), where g_0 becomes important and favors the plane-wave phases at large $|m_z|$. In Fig. 4(a), we plot the phase diagram in the m_z-g_2/g_0 plane with fixed g_2, and a small m_x is used to obtain a small SO coupling $k_m \sim k_R/4$ (corresponding to a long superstripe period of ≈ 3.2 μm, enough for direct real-space observation [50–52]). We find that even for strong density interaction $|g_2|/g_0 \sim 0.005$ (typical for ^{87}Rb atoms) the long-period, high visibility superstripes can exist up to a
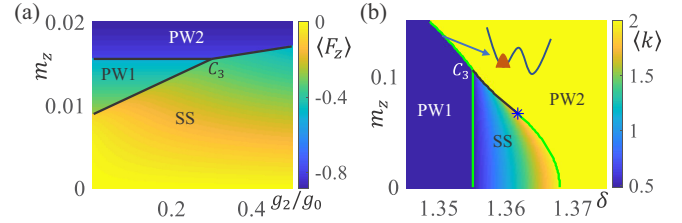
large Zeeman field $|m_z| \sim g_2\bar{n}$ without involving strong total density modulations.

The SS phase becomes more robust against m_z in the strong SO coupling region. Figure 4(b) shows the phase diagram in the m_z-δ plane for $k_m \sim 1.5k_R$ (corresponding to a short superstripe period which may be observed by Bragg reflection). The system may stay in the SS phase until it shrinks to the triple point C_3 at extremely strong Zeeman field $m_z \sim 10g_2\bar{n}$. The transition order can be revealed by looking at the behavior of $\langle k \rangle$, $\langle F_z \rangle$, or the visibility (i.e., a jump in $\langle k \rangle$, $\langle F_z \rangle$, or visibility represents a first-order transition). It is worth mentioning that for $m_z \neq 0$ the Hamiltonian no longer has the symmetry between $|\uparrow\rangle$ and $|\downarrow\rangle$, and all phases have nonzero $\langle F_z \rangle$. As a result, the phase transitions between PPW and PW1 (PW2) become crossovers (see the Appendix).

Due to the hybridization between $|+\rangle$ and $|0\rangle$ for the $|\uparrow'\rangle$ band, m_z would lower the right minimum more significantly. Therefore the global minimum may change from left to right as we increase m_z, which drives the phase transitions from the SS phase first to the PW1 phase and then to the PW2 phase [see the left part in Fig. 4(a)]. In addition, the transition from PW2 to PW1 occurs when the global band minimum is still the right one, which means that the BEC prefers the high-energy local minimum at the left [as schematically shown in the inset of Fig. 4(b)], where the hybridization between $|+\rangle$ and $|0\rangle$ leads to a lower interaction energy from $g_2 n_0 (n_\uparrow + n_\downarrow)$ that compensates the higher single-particle energy.

VI. CONCLUSIONS

In summary, we propose a scheme to realize a magnetic superstripe phase through engineering a spin-1/2 subsystem with tunable SO coupling in a spin-1 BEC. The tunable SO coupling could be generalized to other Bose and Fermi cold atomic systems, including alkaline-earth(-like) atoms. The system does not suffer heating issues and is robust against magnetic-field fluctuations, making it a promising platform to explore supersolid physics (e.g., the phase transition, nontrivial dynamics, and the roton spectrum). More importantly, the superstripe phase has magnetic crystalline structure with a high visibility and long tunable period that can be directly
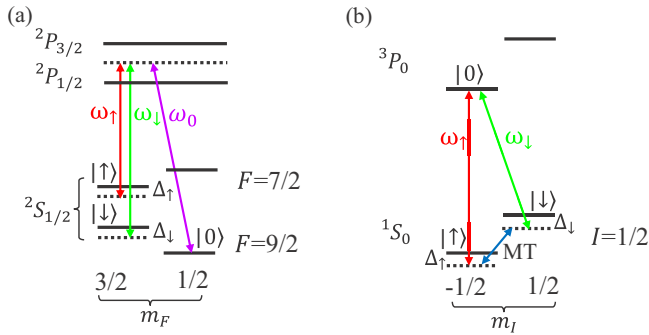
FIG. 5. (a) Energy levels and Raman transitions to generate tunable SO coupling for ^{40}K. (b) Energy levels and clock (microwave) transitions to generate tunable SO coupling for ^{171}Yb.

detected by real-space imaging. Our scheme not only opens the possibility for exploring novel physics with tunable SO coupling, but also paves the way for conclusive (real-space) observation and exploration of long-sought supersolid phases in experiments.

APPENDIX

1. Other experimental configurations for generating tunable SO coupling

Our scheme for tunable 1D SO coupling only relies on the existence of three hyperfine ground states that can be coupled with each other, therefore it can be applied to other alkali-metal (e.g., potassium) and alkaline-earth(-like) atoms (e.g., strontium and ytterbium). The corresponding laser configurations could be slightly different.

For instance, for fermionic ^{40}K, we can choose $|\downarrow\rangle = |F = \frac{7}{2}, m_F = \frac{3}{2}\rangle$, $|\uparrow\rangle = |F = \frac{9}{2}, m_F = \frac{3}{2}\rangle$, and $|0\rangle = |F = \frac{9}{2}, m_F = \frac{1}{2}\rangle$ as the spin states [24] [Fig. 5(a)] with the same laser configuration as that in Fig. 1(a) in the main text. The phases of these Raman lasers are irrelevant because they can be gauged out in the definition of spin states. The coupling δ between $|\downarrow\rangle$) and $|\uparrow\rangle$ is realized directly by the Raman lasers $\omega_\uparrow$ and $\omega_\downarrow$ [24], and a positive $\delta > 0$ can be obtained using Raman lasers between $D1$ and $D2$ lines (no need for microwave fields). Notice that for ^{87}Rb in the $F = 1$ manifold in the main text the two-photon microwave transition is used to couple $|F = 1, m_F = 1\rangle$ ($|\downarrow\rangle$) and $|F = 1, m_F = -1\rangle$ ($|\uparrow\rangle$) because the corresponding Raman coupling needs to be near resonance, yielding significant heating.

For the fermionic alkaline-earth(-like) atoms (e.g., ^{87}Sr, ^{171}Yb, and ^{173}Yb) [53–56], we can use two nuclear spin states in the $^1S_0$ manifold and one nuclear spin state in the $^3P_0$ manifold to represent a spin-1 system [see Fig. 5(b)]. Instead of a Raman process, the coupling between $|0\rangle$ and

$|\uparrow, \downarrow\rangle$ is realized by the one-photon Rabi transition (i.e., the clock transition). The laser setup is similar to that in Fig. 1 in the main text, except that only two laser beams $\omega_\uparrow$ and $\omega_\downarrow$ are needed, the polarizations of which are rotated by $\pi/4$ with respect to the z direction. These lasers can generate both π- and σ^--clock transitions between $|0\rangle$ and $|\uparrow, \downarrow\rangle$. A one-photon microwave transition is also needed to achieve the coupling between $|\uparrow\rangle$ and $|\downarrow\rangle$. To obtain a positive δ, the phase of the microwave field is locked to the same value as the phase difference between two clock lasers. The couplings with other nuclear spin states are suppressed due to the different Zeeman splitting and dipole potential [53,54]. Similar spin-orbit coupling schemes can also be applied to fermionic species that are not considered in this paper.

2. Variational energy functional

In the basis $\Psi = (\psi_\uparrow, \psi_0, \psi_\downarrow)^T$, the interaction energy in the laboratory frame is

$$\varepsilon_{int} = \frac{1}{V} \int dx \left[\frac{g_0}{2} n^2 + \frac{g_0}{2} (\Psi^\dagger \mathbf{F} \Psi)^2 \right]$$

$$= \frac{1}{V} \int dx \left[\frac{g_0}{2} n^2 + g_2 n_0 (n_\uparrow + n_\downarrow) + \frac{g_2}{2} (n_\uparrow - n_\downarrow)^2 \right]$$

$$+ \frac{1}{V} \int dx 2 g_2 \mathrm{Re}[\psi_\uparrow \psi_\downarrow \psi_0^* \psi_0^*], \tag{A1}$$

where $\mathbf{F} = (F_x, F_y, F_z)$. After the unitary transformation $U = \exp(i2k_R x)|0\rangle\langle 0|$ to the quasimomentum frame, the above equation is unchanged except that the last term becomes

$$\frac{1}{V} \int dx 2 g_2 \mathrm{Re}[\psi_\uparrow \psi_\downarrow \psi_0^* \psi_0^* \times \exp(4 i k_R x)], \tag{A2}$$

which is nonzero only when the state is a superposition of two plane waves with momentum separation $2k_R$. Here we focus on the case where the momentum separation is much smaller than $2k_R$, therefore this term becomes zero and we obtain the interaction energy Eq. (2) in the main text.

Using the variational ansatz

$$\Psi = \sqrt{\bar{n}} |c_1| \begin{pmatrix} \cos(\theta_1) \cos(\phi_1) \\ -\sin(\theta_1) \\ \cos(\theta_1) \sin(\phi_1) \end{pmatrix} e^{ik_1 x} + \sqrt{\bar{n}} |c_2|$$

$$\times \begin{pmatrix} \cos(\theta_2) \cos(\phi_2) \\ -\sin(\theta_2) \\ \cos(\theta_2) \sin(\phi_2) \end{pmatrix} e^{ik_2 x + i\alpha}, \tag{A3}$$

we obtain the single-particle energy density

$$\varepsilon_0 = \frac{1}{V} \int dx \Psi^\dagger H_0 \Psi$$

$$= \bar{n} \sum_i |c_i|^2 \left\{ k_i^2 + \sin(2\theta_i) \sin\left(\phi_i + \frac{\pi}{4} \right) \right.$$

$$\left. + [\Delta + 4 - 4k_i + \delta \sin(2\phi_i) + m_z \cos(2\phi_i)] \cos^2(\theta_i) \right\}, \tag{A4}$$
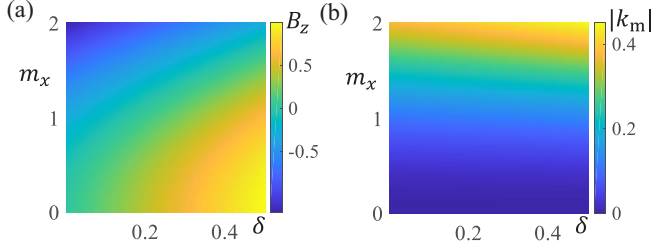
FIG. 6. (a, b) The dependence of B_z and k_m on the Raman and microwave couplings m_x and δ. The parameters are $\Delta = -2$, $m_x = 1$, $\delta = 0.18$, and $m_z = 0$.

FIG. 7. (a, b) The corresponding visibility (v) and period (P) of the spin-density modulations in the SS phase shown in Fig. 1(a) in the main text, with $v \equiv \frac{\max(n_{\uparrow,\downarrow}) - \min(n_{\uparrow,\downarrow})}{\max(n_{\uparrow,\downarrow}) + \min(n_{\uparrow,\downarrow})}$. We set $P = v = 0$ in the (polarized) plane-wave phases, and the maximum period in the SS phase is about 3.8 μm.

and the interaction energy density

$$
\begin{aligned}
\varepsilon_{\text{int}} = \bar{n}\frac{g_0\bar{n}}{2}&\left\{1 + 2|c_1|^2|c_2|^2[\sin(\theta_1)\sin(\theta_2)\right.\\
&+ \cos(\theta_1)\cos(\theta_2)\cos(\phi_1 - \phi_2)]^2\right\}\\
&+ \bar{n}\frac{g_2\bar{n}}{2}\{2|c_1c_2|^2[\cos^2(\theta_1)\cos^2(\theta_2)\cos^2(\phi_1 + \phi_2)\\
&+ \sin(2\theta_1)\sin(2\theta_2)\cos(\phi_1 - \phi_2)]\\
&+ \left[\sum_i |c_i|^2\cos^2(\theta_i)\cos(2\phi_i)\right]^2 + 2\left[\sum_i |c_i|^2\sin^2(\theta_i)\right]\\
&\left.\times\left[\sum_i |c_i|^2\cos^2(\theta_i)\right]\right\},
\end{aligned}
\tag{A5}
$$

with the total-energy density given by $\varepsilon_{\text{tot}} = \varepsilon_0 + \varepsilon_{\text{int}}$.

3. Some details about tunable SO coupling and the superstripe phase

As we discussed in the main text, the low-energy dynamics are characterized by an effective spin-1/2 system with tunable SO coupling, with an effective Hamiltonian (in the basis $\{|\uparrow'\rangle, |\downarrow'\rangle\}$):

$$
H_{\text{eff}} = \begin{bmatrix} \eta(k - k_m)^2 & 0 \\ 0 & k^2 \end{bmatrix} + B_z\sigma_z + B_x\sigma_x.
\tag{A6}
$$

The transverse field B_x is approximately given by the Zeeman field m_z, while the longitudinal field B_z and the SO coupling strength k_m can be tuned by varying Raman and microwave coupling strengths m_x and δ. In Fig. 6, we plot the dependence of B_z and k_m on m_x and δ.

Due to the tunability of the SO coupling, we can obtain superstripe phases with a tunable and long period, and the effects of density interaction can be suppressed by a weak or vanishing B_x, which leads to a high-visibility spin superstripe phase favored by the spin interaction. In Fig. 7, we plot the period and visibility of the superstripe phase in Fig. 1(a) in the main text.

We notice that the SO coupling is written in the basis $|\uparrow'\rangle$ and $|\downarrow'\rangle$ [which are approximately given by $|\uparrow'\rangle \simeq |+\rangle = \frac{1}{\sqrt{2}}(|\uparrow\rangle + |\downarrow\rangle)$ and $|\downarrow'\rangle = |-\rangle = \frac{1}{\sqrt{2}}(|\uparrow\rangle - |\downarrow\rangle)$], while the spin-density modulation is formed in a different basis $|\uparrow\rangle$ and $|\downarrow\rangle$. A natural question to ask is whether high-visibility spin-density modulation can be obtained in the basis $|+\rangle$ and $|-\rangle$ for the conventional SO coupling scheme in the basis $|\uparrow\rangle$ and $|\downarrow\rangle$. The answer is no and the reason is illustrated below. In our scheme, only state $|0\rangle$ is transformed to the
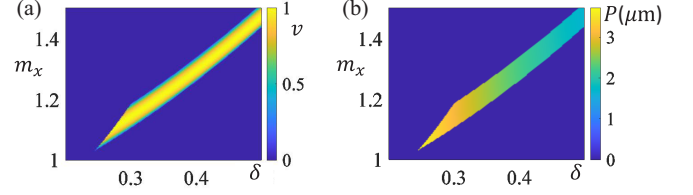
quasimomentum frame, and states $|\uparrow\rangle$ and $|\downarrow\rangle$ are associated with atomic mechanical momentum, therefore the plane-wave superposition of $|+\rangle$ and $|-\rangle$ at different momenta gives rise to spin-density modulation in the laboratory frame, with period directly determined by the momentum difference between two plane waves, while for the conventional SO coupling scheme in the basis $|\uparrow\rangle$ and $|\downarrow\rangle$ both states $|\uparrow\rangle$ and $|\downarrow\rangle$ are transformed to the quasimomentum frame, and the superstripe state in the quasimomentum frame is [14]

$$
(|\uparrow\rangle + \epsilon|\downarrow\rangle)e^{-ikx} + (|\downarrow\rangle + \epsilon|\uparrow\rangle)e^{ikx}.
\tag{A7}
$$

In the ideal case, we may have $k \simeq k_R(1 - g_2/2g_0)$ and $\epsilon \simeq \sqrt{g_2/2g_0}$. After transforming back to the laboratory frame, the above state in the basis $|\pm\rangle$ can be written as

$$
\begin{aligned}
&[\cos(kx - k_Rx) + \epsilon\cos(kx + k_Rx)]|+\rangle\\
&+ [\sin(kx - k_Rx) + \epsilon\sin(kx + k_Rx)]|-\rangle.
\end{aligned}
\tag{A8}
$$

Without loss of generality, we consider the $|+\rangle$ state, where $\epsilon\cos(kx + k_Rx)$ gives a short-period modulation (≈ 0.4 μm) with a low visibility $\approx \sqrt{g_2/2g_0}$ that is around 5% for typical parameters of ^{87}Rb, while $\cos(kx - k_Rx)$ gives an extremely long-period modulation around 300 μm that is invisible for typical BEC cloud size (less than 100 μm).
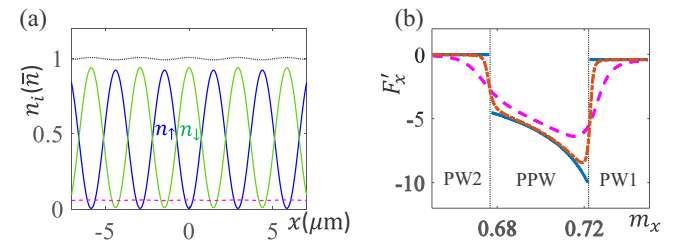

FIG. 8. (a) Spin-density modulation in the SS phase with $\delta = 0.3$ and $m_z = 0.8g_2\bar{n}$. Both the total density and spin densities have slight periodic modulations. Other parameters are the same as Fig. 4(a) in the main text. (b) Change from second-order phase transitions to crossovers due to finite Zeeman field m_z. From the first-order derivative of F_x over m_x (which equals to the second-order derivative of ε_{tot} over m_x due to the Hellmann-Feynman theorem, i.e., $F_x' = \varepsilon_{\text{tot}}''$), we see that that The PPW-PW1 and PPW-PW2 boundaries change from second-order boundaries with $m_z = 0$ (blue solid line) to crossover boundaries with $m_z \neq 0$ (red dash-dotted line for $m_z = 10^{-4}$ and purple dashed line for $m_z = 10^{-3}$). Other parameters are $\Delta = -1$ and $\delta = 0.1$.

In the presence of m_z (i.e., $B_x \neq 0$), the spin states at two band minima are no longer orthogonal, and the SS phase now possesses both spin-density and total density modulations, as shown in Fig. 8(a). The Zeeman field m_z breaks the Z_2 sym-

metry between $|\uparrow\rangle$ and $|\downarrow\rangle$, and all phases now have nonzero $\langle F_z \rangle$. The phase transitions between PPW and PW1 (PW2) become crossovers, as confirmed by our numerical results of the derivative of the ground-state energy [see Fig. 8(b)].

[1] M. Boninsegni and N. V. Prokof'ev, Colloquium: Supersolids: What and where are they? Rev. Mod. Phys. **84**, 759 (2012).

[2] D. J. Thouless, The flow of a dense superfluid, Ann. Phys. (NY) **52**, 403 (1969).

[3] A. F. Andreev and I. M. Lifshitz, Quantum theory of defects in crystals, Sov. Phys. JETP **29**, 1107 (1969).

[4] F. Cinti, T. Macrí, W. Lechner, G. Pupillo, and T. Pohl, Defect-induced supersolidity with soft-core bosons, Nat. Commun. **5**, 3235 (2014).

[5] K. Baumann, C. Guerlin, F. Brennecke, and T. Esslinger, Dicke quantum phase transition with a superfluid gas in an optical cavity, Nature (London) **464**, 1301 (2010).

[6] H. Keßler, J. Klinder, M. Wolke, and A. Hemmerich, Steering Matter Wave Superradiance with an Ultranarrow-Band Optical Cavity, Phys. Rev. Lett. **113**, 070404 (2014).

[7] J. Léonard, A. Morales, P. Zupancic, T. Esslinger, and T. Donner, Supersolid formation in a quantum gas breaking a continuous translational symmetry, Nature (London) **543**, 87 (2017).

[8] L. Tanzi, E. Lucioni, F. Famá, J. Catani, A. Fioretti, C. Gabbanini, R. N. Bisset, L. Santos, and G. Modugno, Observation of a Dipolar Quantum Gas with Metastable Supersolid Properties, Phys. Rev. Lett. **122**, 130405 (2019).

[9] F. Böttcher, J.-N. Schmidt, M. Wenzel, J. Hertkorn, M. Guo, T. Langen, and T. Pfau, Transient Supersolid Properties in an Array of Dipolar Quantum Droplets, Phys. Rev. X **9**, 011051 (2019).

[10] L. Chomaz, D. Petter, P. Ilzhöfer, G. Natale, A. Trautmann, C. Politi, G. Durastante, R. M. W. van Bijnen, A. Patscheider, M. Sohmen, M. J. Mark, and F. Ferlaino, Long-Lived and Transient Supersolid Behaviors in Dipolar Quantum Gases, Phys. Rev. X **9**, 021012 (2019).

[11] C. Wang, C. Gao, C. Jian, and H. Zhai, Spin-Orbit Coupled Spinor Bose-Einstein Condensates, Phys. Rev. Lett. **105**, 160403 (2010).

[12] T.-L. Ho and S. Zhang, Bose-Einstein Condensates with Spin-Orbit Interaction, Phys. Rev. Lett. **107**, 150403 (2011).

[13] Y. Zhang, L. Mao, and C. Zhang, Mean-Field Dynamics of Spin-Orbit Coupled Bose-Einstein Condensates, Phys. Rev. Lett. **108**, 035302 (2012).

[14] Y. Li, L. Pitaevskii, and S. Stringari, Quantum Tricriticality and Phase Transitions in Spin-Orbit Coupled Bose-Einstein Condensates, Phys. Rev. Lett. **108**, 225301 (2012).

[15] Y. Li, G. Martone, L. Pitaevskii, and S. Stringari, Superstripes and the Excitation Spectrum of a Spin-Orbit-Coupled Bose-Einstein Condensate, Phys. Rev. Lett. **110**, 235302 (2013).

[16] Y.-J. Lin, K. Jiménez-García, and I. B. Spielman, Spin-orbit-coupled Bose-Einstein condensates, Nature (London) **471**, 83 (2011).

[17] J.-Y. Zhang S.-C. Ji, Z. Chen, L. Zhang, Z.-D. Du, B. Yan, G.-S. Pan, B. Zhao, Y.-J. Deng, H. Zhai, S. Chen, and J.-W. Pan,

Collective Dipole Oscillations of a Spin-Orbit Coupled Bose-Einstein Condensate, Phys. Rev. Lett. **109**, 115301 (2012).

[18] C. Qu, C. Hamner, M. Gong, C. Zhang, and P. Engels, Observation of zitterbewegung in a spin-orbit-coupled Bose-Einstein condensate, Phys. Rev. A **88**, 021604 (2013).

[19] S.-C. Ji, J.-Y. Zhang, L. Zhang, Z.-D. Du, W. Zheng, Y.-J. Deng, H. Zhai, S. Chen, and J.-W. Pan, Experimental determination of the finite-temperature phase diagram of a spin-orbit coupled Bose gas, Nat. Phys. **10**, 314 (2014).

[20] A. Olson, S. Wang, R. Niffenegger, C. Li, C. Greene, and Y. Chen, Tunable landau-zener transitions in a spin-orbit-coupled Bose-Einstein condensate, Phys. Rev. A **90**, 013616 (2014).

[21] P. Wang, Z.-Q. Yu, Z. Fu, J. Miao, L. Huang, S. Chai, H. Zhai, and J. Zhang, Spin-Orbit Coupled Degenerate Fermi Gases, Phys. Rev. Lett. **109**, 095301 (2012).

[22] L. Cheuk, A. Sommer, Z. Hadzibabic, T. Yefsah, W. Bakr, and M. Zwierlein, Spin-Injection Spectroscopy of a Spin-Orbit Coupled Fermi Gas, Phys. Rev. Lett. **109**, 095302 (2012).

[23] R. A. Williams, M. C. Beeler, L. J. LeBlanc, K. Jiménez-García, and I. B. Spielman, Raman-Induced Interactions in a Single-Component Fermi Gas Near an *s*-Wave Feshbach Resonance, Phys. Rev. Lett. **111**, 095301 (2013).

[24] L. Huang, Z. Meng, P. Wang, P. Peng, S.-L. Zhang, L. Chen, D. Li, Q. Zhou, and J. Zhang, Experimental realization of two-dimensional synthetic spin-orbit coupling in ultracold fermi gases, Nat. Phys. **12**, 540 (2016).

[25] Z. Wu, L. Zhang, W. Sun, X.-T. Xu, B.-Z. Wang, S.-C. Ji, Y. Deng, S. Chen, X.-J. Liu, and J.-W. Pan, Realization of two-dimensional spin-orbit coupling for Bose-Einstein condensates, Science **354**, 83 (2016).

[26] D. Campbell, R. Price, A. Putra, A. Valdés-Curiel, D. Trypogeorgos, and I. B. Spielman, Magnetic phases of spin-1 spin-orbit-coupled Bose gases, Nat. Commun. **7**, 10897 (2016).

[27] X. Luo, L. Wu, J. Chen, Q. Guan, K. Gao, Z.-F. Xu, L. You, and R. Wang, Tunable atomic spin-orbit coupling synthesized with a modulating gradient magnetic field, Sci. Rep. **6**, 18983 (2016).

[28] T. D. Stanescu, B. Anderson, and V. Galitski, Spin-orbit coupled Bose-Einstein condensates, Phys. Rev. A **78**, 023616 (2008).

[29] C. Wu, I. Mondragon-Shem, and X.-F. Zhou, Unconventional bose-einstein condensations from spin-orbit coupling, Chin. Phys. Lett. **28**, 097102 (2011).

[30] H. Hu, B. Ramachandhran, H. Pu, and X. Liu, Spin-Orbit Coupled Weakly Interacting Bose-Einstein Condensates in Harmonic Traps, Phys. Rev. Lett. **108**, 010402 (2012).

[31] T. Ozawa and G. Baym, Stability of Ultracold Atomic Bose Condensates with Rashba Spin-Orbit Coupling Against Quantum and Thermal Fluctuations, Phys. Rev. Lett. **109**, 025301 (2012).

[32] Z. Lan and P. Öhberg, Raman-dressed spin-1 spin-orbit-coupled quantum gas, Phys. Rev. A **89**, 023630 (2014).

[33] S. S. Natu, X. Li, and W. S. Cole, Striped ferronematic ground states in a spin-orbit-coupled $S = 1$ Bose gas, Phys. Rev. A **91**, 023608 (2015).

[34] V. Galitski and I. B. Spielman, Spin-orbit coupling in quantum gases, Nature (London) **494**, 49 (2013).

[35] J. Li, W. Huang, B. Shteynas, S. Burchesky, F. çağrı Top, E. Su, J. Lee, A. O. Jamison, and W. Ketterle, Spin-Orbit Coupling and Spin Textures in Optical Superlattices, Phys. Rev. Lett. **117**, 185301 (2016).

[36] J.-R. Li, J. Lee, W. Huang, S. Burchesky, B. Shteynas, F. Çağrı Top, A. O. Jamison, and W. Ketterle, A stripe phase with supersolid properties in spin–orbit-coupled Bose-Einstein condensates, Nature (London) **543**, 91 (2017).

[37] G. Martone, Y. Li, and S. Stringari, Approach for making visible and stable stripes in a spin-orbit-coupled Bose-Einstein superfluid, Phys. Rev. A **90**, 041604(R) (2014).

[38] T.-L. Ho, Spinor Bose Condensates in Optical Traps, Phys. Rev. Lett. **81**, 742 (1998).

[39] T. Ohmi and K. Machida, Bose-Einstein condensation with internal degrees of freedom in alkali atom gases, J. Phys. Soc. Jpn. **67**, 1822 (1998).

[40] K. Sun, C. Qu, Y. Xu, Y. Zhang, and C. Zhang, Interacting spin-orbit-coupled spin-1 Bose-Einstein condensates, Phys. Rev. A **93**, 023615 (2016).

[41] Z.-Q. Yu, Phase transitions and elementary excitations in spin-1 Bose gases with Raman-induced spin-orbit coupling, Phys. Rev. A **93**, 033648 (2016).

[42] G. Martone, F. Pepe, P. Facchi, S. Pascazio, and S. Stringari, Tricriticalities and Quantum Phases in Spin-Orbit-Coupled Spin-1 Bose Gases, Phys. Rev. Lett. **117**, 125301 (2016).

[43] X.-W. Luo, K. Sun, and C. Zhang, Spin-Tensor–Momentum-Coupled Bose-Einstein Condensates, Phys. Rev. Lett. **119**, 193001 (2017).

[44] M. R. Matthews, D. S. Hall, D. S. Jin, J. R. Ensher, C. E. Wieman, E. A. Cornell, F. Dalfovo, C. Minniti, and S. Stringari, Dynamical Response of a Bose-Einstein Condensate to a Discontinuous Change in Internal State, Phys. Rev. Lett. **81**, 243 (1998).

[45] K. M. Mertes, J. W. Merrill, R. Carretero-González, D. J. Frantzeskakis, P. G. Kevrekidis, and D. S. Hall, Nonequilibrium Dynamics and Superfluid Ring Excitations in Binary Bose-Einstein Condensates, Phys. Rev. Lett. **99**, 190402 (2007).

[46] M. Egorov, B. Opanchuk, P. Drummond, B. V. Hall, P. Hannaford, and A. I. Sidorov, Measurement of s-wave scattering lengths in a two-component Bose-Einstein condensate, Phys. Rev. A **87**, 053614 (2013).

[47] Y. Zhang, G. Chen, and C. Zhang, Tunable spin-orbit coupling and quantum phase transition in a trapped bose-einstein condensate, Sci. Rep. **3**, 1937 (2013).

[48] K. Jiménez-García, L. J. LeBlanc, R. A. Williams, M. C. Beeler, C. Qu, M. Gong, C. Zhang, and I. B. Spielman, Tunable Spin-Orbit Coupling via Strong Driving in Ultracold-Atom Systems, Phys. Rev. Lett. **114**, 125301 (2015).

[49] F. Grusdt, T. Li, I. Bloch, and E. Demler, Tunable spin-orbit coupling for ultracold atoms in two-dimensional optical lattices, Phys. Rev. A **95**, 063617 (2017).

[50] L. LeBlanc, M. Beeler, K. Jiménez-García, A. Perry, S. Sugawa, R. Williams, and I. Spielman, Direct observation of zitterbewegung in a Bose-Einstein condensate, New J. Phys. **15**, 073011 (2013).

[51] M. Leder, C. Grossert, L. Sitta, M. Genske, A. Rosch, and M. Weitz, Real-space imaging of a topologically protected edge state with ultracold atoms in an amplitude-chirped optical lattice, Nat. Commun. **7**, 13112 (2016).

[52] M. Parsons, F. Huber, A. Mazurenko, C. Chiu, and W. Setiawan, Site-Resolved Imaging of Fermionic ⁶Li in an Optical Lattice, Phys. Rev. Lett. **114**, 213002 (2015).

[53] M. Boyd, T. Zelevinsky, A. Ludlow, S. Blatt, T. Zanon-Willette, S. Foreman, and J. Ye, Nuclear spin effects in optical lattice clocks, Phys. Rev. A **76**, 022510 (2007).

[54] M. Mancini, G. Pagano, G. Cappellini, L. Livi, M. Rider, J. Catani, C. Sias, P. Zoller, M. Inguscio, M. Dalmonte, and L. Fallani, Observation of chiral edge states with neutral fermions in synthetic Hall ribbons, Science **349**, 1510 (2015).

[55] S. Kolkowitz, S. Bromley, T. Bothwell, M. Wall, G. Marti, A. Koller, X. Zhang, A. Rey, and J. Ye, Spin–orbit-coupled fermions in an optical lattice clock, Nature **542**, 66 (2017).

[56] S. Bromley, S. Kolkowitz, T. Bothwell, D. Kedar, A. Safavi-Naini, M. Wall, C. Salomon, A. Rey, and J. Ye, Dynamics of interacting fermions under spin–orbit coupling in an optical lattice clock, Nat. Phys. **14**, 399 (2018).